Asymptotic-preserving schemes for kinetic–fluid modeling of disperse two-phase flows with variable fluid density

Thierry Goudon[1], Shi Jin[2,3,*,†], Jian-Guo Liu[4] and Bokai Yan[5]

[1]*Team COFFEE, INRIA Sophia Antipolis Méditerranée and Labo. J. A. Dieudonné UMR 6621 CNRS & Université Nice Sophia Antipolis, Nice, France*
[2]*Department of Mathematics, Institute of Natural Sciences, and Ministry of Education Key Laboratory of Scientific and Engineering Computing, Shanghai Jiao Tong University, Shanghai 200240, China*
[3]*Department of Mathematics, University of Wisconsin-Madison, Madison, WI 53706, USA*
[4]*Department of Physics and Department of Mathematics, Duke University, Durham, NC 27708, USA*
[5]*Department of Mathematics, University of California, Los Angeles, Los Angeles, CA 90034, USA*

SUMMARY

We are concerned with a coupled system describing the interaction between suspended particles and a dense fluid. The particles are modeled by a kinetic equation of Vlasov–Fokker–Planck type, and the fluid is described by the incompressible Navier–Stokes system, with variable density. The systems are coupled through drag forces. High friction regimes lead to a purely hydrodynamic description of the mixture. We design first and second order asymptotic-preserving schemes suited to such regimes. We extend the method introduced in [Goudon T, Jin S, Liu JG, Yan B. *Journal of Computational Physics* 2013; **246**:145-164] to the case of variable density in compressible flow. We check the accuracy and the asymptotic-preserving property numerically. We set up a few numerical experiments to demonstrate the ability of the scheme in capturing intricate interactions between the two phases on a wide range of physical parameters and geometric situations. Copyright © 2014 John Wiley & Sons, Ltd.

Received 16 December 2011; Revised 13 November 2013; Accepted 19 January 2014

KEY WORDS: fluid–particles flows; hydrodynamic regimes; asymptotic-preserving schemes; kinetic-fluid model; variable density incompressible flow

1. INTRODUCTION

This paper is devoted to the numerical study of a disperse two-phase flow. It includes the dilute particles and the surrounding fluid in which the particles are suspended. The particles are modeled at the mesoscopic level, therefore described by a kinetic equation, the unknown of which is the distribution function $f(t,x,v)$ defined in the phase space $(x,v) \in \mathbb{R}^N \times \mathbb{R}^N$. The fluid is modeled by the incompressible Navier–Stokes (INS) system, describing the evolution of the density $\rho(t,x)$, velocity field $u(t,x)$, and pressure $p(t,x)$ of the dense phase. By contrast to the particle distribution function, these unknowns only depend on the time and space variables. The mathematical model is based on the following assumptions:

- The fluid is viscous and incompressible, with variable density.
- Both the fluid and particle phases are isothermal with temperature $T = 1$.
- We consider a single specie of particles, with given and fixed mass density. We assume that particles are spherically shaped with a given and fixed radius. We neglect any coagulation and break–up phenomena.

*Correspondence to: Shi Jin, Department of Mathematics, Institute of Natural Sciences, and Ministry of Education Key Laboratory of Scientific and Engineering Computing, Shanghai Jiao Tong University, Shanghai 200240, China.
†E-mail: jin@math.wisc.edu

- There is no mass exchange between the phases. The volume fraction occupied by the particles does not influence significantly the fluid density. Each phase exerts an influence on the other phase through drag forces. The Stokes formula is used: the drag force depends linearly on the relative velocity $(v-u)$.
- Particles are subject to Brownian motion, which leads to diffusion with respect to the velocity variable in the equation of the particle distribution function.

With these assumptions in hands, we can write down the equations for this system. The evolution of the particle distribution function f obeys the Vlasov–Fokker–Planck type kinetic equation

$$\partial_t f + v\cdot\nabla_x f = \frac{1}{\varepsilon} L_u f + \nabla_x \Phi\cdot\nabla_v f, \tag{1}$$

with the Fokker–Planck operator

$$L_u f = \nabla_v\cdot((v-u)f + \nabla_v f) = \nabla_v\cdot\left(M_u\nabla_v\left(\frac{f}{M_u}\right)\right). \tag{2}$$

Here and later, we denote

$$M_u(v) = \frac{1}{(2\pi)^{N/2}}\exp\left(-\frac{|v-u|^2}{2}\right)$$

the (normalized) Maxwellian centered at u (that can be a function of t and x). The density $\rho(t,x)$ and velocity $u(t,x)$ of the fluid are governed by the INS system

$$\begin{cases} \partial_t\rho + \nabla_x\cdot(\rho u) = 0 \\ \partial_t(\rho u) + \nabla_x\cdot(\rho u\otimes u) + \nabla_x p - \dfrac{1}{\mathrm{Re}}\Delta_x u + \rho\nabla_x\Psi = \dfrac{\kappa}{\varepsilon}\displaystyle\int (v-u)f\,\mathrm{d}v, \\ \nabla_x\cdot u = 0. \end{cases} \tag{3}$$

The pressure $p(t,x)$ is determined by the divergence free condition. The readers are referred to [1] and the references therein for the projection methods on variable density INS system.

In (3), $\mathrm{Re} > 0$ is the fluid Reynolds number. The coupling parameter is defined by $\kappa = \bar{\phi}\rho_P/\rho_F$, where $\bar{\phi}$ is the (typical value of the) volume fraction of particles, and ρ_F and ρ_P are the (typical) mass densities of the fluid and the particles, respectively. For most applications, ρ_P is much bigger than ρ_F, but $\bar{\phi}$ is very small under our assumptions, and we can neglect the fluid volume change because of the presence of particles. Thus, κ is the mass ratio between particles and fluid in a given reference volume. We will assume that κ is $O(1)$, so the influence from both phases to the other are significant. The two phases are subject to external potentials Φ and Ψ. The external force might be different for the two phases. For example in the case of gravity driven flows, the potentials are given by $\Phi = \eta_P g e_z$ and $\Psi = \eta_F g e_z$, with e_z the unit downward vector and g the gravitational acceleration. For the particles, the coefficient $\eta_P = (1-\rho_F/\rho_P)$ accounts for the gravity and buoyancy force. For the fluid, the coefficient is just $\eta_F = 1$ because of the effect of gravity. Finally, the scaling parameter $0 < \varepsilon \ll 1$ is the ratio of the Stokes settling time to the observation time. The Stokes settling time is given by $\tau = \frac{2a^2\rho_P}{9\mu}$, with a the particle radius and μ the fluid viscosity. In a typical soot, $\tau \approx 10^{-8}$ s. We refer to [2] for details.

Flows described by such models typically arise in combustion theory [3–6], for describing pollutant dispersion [7, 8], or the dynamics or sprays with, for example, biomedical applications [9, 10]. Here, the model belongs to the so-called thin sprays models [5]. As it is usual with multiphase flows, several modeling assumptions might be questionable; however, any modification can drastically impact both the mathematical properties of the models and their numerical treatment, as pointed out in [11]. As we shall see later, regimes with $0 < \varepsilon \ll 1$ introduce relaxation effects that drive the particle distribution function towards a Maxwellian state. In turn, the flow can be described through macroscopic quantities depending only on time and space variables. We refer to [2, 12–14] for details on the scaling issues and for further references on the analysis of such asymptotic regimes.

DOI: 10.1002/fld

Owing to the divergence free condition satisfied by u, we observe that the fluid density is constant on the characteristic curves associated to the field u: as far as the velocity field is smooth enough, let $X(t,x)$ be the solution of

$$\dot{X}(t,x) = u(t, X(t,x)), \qquad X(0,x) = x$$

so that the mass conservation relation implies

$$\frac{\mathrm{d}}{\mathrm{d}t}\rho(t, X(t,x)) = 0.$$

Consequently, assuming that the dense phase is initially homogeneous, it remains homogeneous forever: if $\rho\,|_{t=0} = \bar{\rho} > 0$ is constant, then $\rho(t,x) = \bar{\rho}$. This specific situation is investigated in the companion paper [1]. However, the restriction to homogeneous fluid flows is unrealistic for most of the applications of practical interest. For instance, inhomogeneities play a crucial role in the comprehension of instabilities observed in fluidized beds, technical devices used in pebble bed reactors, and many other industrial processes. The problem combines several technical difficulties. On the one hand, the INS system couples transport and diffusion equations in a very intricate way, together with the divergence free constraint. On the other hand, the coupling with the particles should be incorporated consistently, taking into account the possible stiffness of the coupling force terms. Addressing these difficulties is the object of the present work.

To start with, let us summarize a few remarkable properties of the system and describe formally the behavior as ε goes to 0. A key feature of the model relies on the following energy–entropy dissipation property

$$\begin{aligned}\frac{\mathrm{d}}{\mathrm{d}t}\left(\kappa\int_{\mathbb{R}^N\times\mathbb{R}^N} f(1+\Phi+v^2/2+\ln(f))\,\mathrm{d}v\,\mathrm{d}x + \int_{\mathbb{R}^N}\rho(1+|u|^2/2+\Psi)\,\mathrm{d}x\right)\\ + \frac{1}{\mathrm{Re}}\int_{\mathbb{R}^N}|\nabla_x u|^2\,\mathrm{d}x + \frac{\kappa}{\varepsilon}\int_{\mathbb{R}^N\times\mathbb{R}^N}|(v-u)\sqrt{f} + 2\nabla_v\sqrt{f}|^2\,\mathrm{d}v\,\mathrm{d}x \leqslant 0.\end{aligned} \tag{4}$$

For completeness, we give the proof in the Appendix. This relation also holds when the problem is set on a bounded smooth domain Ω with suitable boundary conditions, for example assuming no-slip of the fluid at the boundary

$$u\Big|_{\partial\Omega} = 0 \tag{5}$$

and specular reflection of the particles

$$\gamma^- f(t,x,v) = \gamma^+ f(t,x,v - 2v\cdot\hat{\nu}(x)\hat{\nu}(x)), \tag{6}$$

where $\hat{\nu}(x)$ is the unit outer normal vector at $x\in\partial\Omega$ and $\gamma^\pm$ are the trace operators on the set

$$\left\{(t,x,v)\in(0,\infty)\times\partial\Omega\times\mathbb{R}^N,\quad \pm v\cdot\hat{\nu}(x) > 0\right\}.$$

We refer to further comments in [13, 14].

By taking the moments of (1), one obtains

$$\partial_t n + \nabla_x\cdot J = 0, \tag{7}$$

$$\partial_t J + \nabla_x\mathbb{P} + n\nabla_x\Phi = -\frac{1}{\varepsilon}(J - nu) \tag{8}$$

where

$$\begin{aligned} n(t,x) &= \int_{\mathbb{R}^N} f(t,x,v)\,\mathrm{d}v,\\ J(t,x) &= \int_{\mathbb{R}^N} vf(t,x,v)\,\mathrm{d}v,\\ \mathbb{P}(t,x) &= \int_{\mathbb{R}^N} v\otimes vf(t,x,v)\,\mathrm{d}v\end{aligned} \tag{9}$$

DOI: 10.1002/fld

are the particle density, momentum, and pressure tensor, respectively. Combined with (3), one arrives at

$$\partial_t(\rho u + \kappa J) + \nabla_x \cdot (\rho u \otimes u + \kappa \mathbb{P}) + \nabla_x p + \kappa n \nabla_x \Phi + \rho \nabla_x \Psi = \frac{1}{\mathrm{Re}} \Delta_x u. \tag{10}$$

The hydrodynamic limit of this system can now be derived. As $\varepsilon \to 0$, one can expect that $L_u f$ (and the dissipation term in (4)) vanishes, which means that f approaches to the Maxwellian centered at the fluid velocity

$$f(t, x, v) \to n(t, x) M_{u(t,x)}(v), \quad \text{as } \varepsilon \to 0.$$

In this regime, the behavior of the particles is therefore described through the evolution of the velocity u and the macroscopic density n. Accordingly, J and $\mathbb{P}$ are asymptotically defined by the moments of the Maxwellian nM_u,

$$J \simeq nu, \qquad \mathbb{P} \simeq nu \otimes u + n\mathbb{I}.$$

Inserting this ansatz into (10), one arrives at the fluid limit

$$\begin{cases} \partial_t \rho + \nabla_x \cdot (\rho u) = 0, \\ \partial_t n + \nabla_x \cdot (nu) = 0, \\ \partial_t((\rho + \kappa n)u) + \nabla_x \cdot ((\rho + \kappa n)u \otimes u) + \nabla_x(p + \kappa n) + \kappa n \nabla_x \Phi + \rho \nabla_x \Psi = \dfrac{1}{\mathrm{Re}} \Delta_x u, \\ \nabla_x \cdot u = 0. \end{cases} \tag{11}$$

Up to the force terms, this system is the INS system for the composite variable density $(\rho + \kappa n)$. Observe that, even if the dense phase is homogeneous, the asymptotic model involves a variable density in the momentum equation. Note that in general, the force term does not reduce to $(\rho + \kappa n)\nabla_x \Psi$. For example, for gravity driven flows, a discrepancy appear because of the buoyancy force that acts on the particles only.

In this paper, we are interested in numerical approximation of the system (1)–(3). We will pay particular attention to the scaling parameter ε: the scheme should work on a wide range of values of the parameter, capturing the expected asymptotic behavior without introducing restrictions that would make small ε's simulations numerically prohibitive. This scheme consists in discretizing implicitly the stiff terms within the equations, but it should be performed as simply as possible because the inversion of the corresponding discrete systems will be the main source of numerical cost. It requires to adapt the ideas in [1] in order to incorporate correctly the treatment of the fluid density. We mention that a rigorous justification of the asymptotic limit is not available yet. We refer to [15] and [13, 16, 17] where related questions are discussed.

The scheme we develop can capture the fluid dynamic limit (11) *automatically* when $\epsilon \to 0$. This is the so-called asymptotic-preserving (AP) property, a term first introduced by Jin [18]. An AP scheme is efficient in the fluid dynamic regime ($\epsilon \ll 1$) because it allows one to capture the fluid dynamic limit (11) without numerically resolving the small scale ϵ. We refer to [19] for a recent review on the AP schemes and their applications. Different from [1], here, we need to develop the scheme in the framework of projection method for variable density INS, which requires different spatial discretization. The overall cost is comparable to solving one decoupled Vlasov–Fokker–Planck equation, see [20], and an INS by the projection method independently.

This work is organized as follows. The AP schemes for the coupling system (1)–(3) are introduced in Section 2. In Section 3, we give the numerical verification of accuracy and the AP property, as well as some relevant applications, which bring out the inhomogeneities effects.

2. ASYMPTOTIC-PRESERVING SCHEMES FOR THE FLUID–PARTICLES SYSTEM

2.1. A first order asymptotic-preserving scheme

Following the first order scheme introduced in [1], the key principles to construct AP schemes can be summarized as follows:

DOI: 10.1002/fld

- Combine the implicit–explicit technique and the pressureless step to update the macroscopic quantities n, J, ρ, u, p by solving directly simple linear systems.
- Split the stiff coupling terms (i.e., $1/\varepsilon$ terms) and distribute them to both the pressureless step and the projection step.
- Solve the stiff terms fully implicitly.
- Apply the prediction–correction idea to update the distribution f, by solving implicitly the Fokker–Planck operator.

We now give the details to update the numerical unknowns, having at hand ρ^k, u^k, p^k, f^k and thus $n^k = \int f^k \mathrm{d}v$, $J^k = \int v f^k \mathrm{d}v$

Step 1: Advancing densities. Both the particles and fluid density are advanced by using the following relations

$$\begin{aligned} \frac{1}{\Delta t}\left(n^{k+1} - n^k\right) &= -\int v \cdot \nabla_x f^k \,\mathrm{d}v, \\ \frac{1}{\Delta t}\left(\rho^{k+1} - \rho^k\right) &= -\nabla_x \cdot \left(\rho^k u^k\right). \end{aligned} \tag{12}$$

Step 2: Updating moments. The macroscopic current J and the velocity field u are advanced by considering the system made of (8) and the second equation of (3). The projection method is applied to account for the divergence free constraint. In order to ensure the AP property, one needs to impose the stiff coupling terms in both the pressureless and the projection steps. To this end, we introduce a parameter $0 < \alpha < 1$ and

Step 2.1: Pressureless step. Obtaining u^* and J^* by solving

$$\frac{1}{\Delta t}\left(J^* - J^k\right) = -\int v \otimes v \nabla_x f^k \,\mathrm{d}v - n^k \nabla_x \Phi - \frac{1-\alpha}{\varepsilon}\left(J^* - n^{k+1}u^*\right), \tag{13a}$$

$$\frac{1}{\Delta t}\left(\rho^{k+1}u^* - \rho^k u^k\right) - \frac{1}{\mathrm{Re}}\Delta_x u^* = -\nabla_x \cdot \left(\rho^k u^k \otimes u^k\right) + \frac{1-\alpha}{\varepsilon}\kappa\left(J^* - n^{k+1}u^*\right). \tag{13b}$$

One is thus led to solve the following variable coefficient Helmholtz equation for u^*

$$\left(\frac{\rho^{k+1}}{\Delta t} + \frac{1-\alpha}{\varepsilon + (1-\alpha)\Delta t}\kappa n^{k+1} - \frac{1}{\mathrm{Re}}\Delta_x\right)u^* = \frac{\rho^k u^k}{\Delta t} - \nabla_x \cdot \left(\rho^k u^k \otimes u^k\right) + \frac{(1-\alpha)\kappa}{\varepsilon + (1-\alpha)\Delta t} \times \left(J^k - \Delta t \int v \otimes v \nabla_x f^k \,\mathrm{d}v - \Delta t n^k \nabla_x \Phi\right), \tag{14}$$

completed with the no-slip boundary condition

$$u^*|_{\partial\Omega} = 0. \tag{15}$$

The discrete Helmholtz operator gives a symmetric linear system that can be solved by the Preconditioned Conjugate Gradient method, see [21]. Then, J^* is updated from (13a).

Step 2.2: Projection step. Calculating J^{**} and u^{k+1} by the relation

$$\begin{aligned} \frac{1}{\Delta t}\left(J^{**} - J^*\right) &= -\frac{\alpha}{\varepsilon}\left(J^{**} - n^{k+1}u^{k+1}\right), \\ \frac{\rho^{k+1}}{\Delta t}\left(u^{k+1} - u^*\right) + \nabla_x p^{k+1} &= \frac{\alpha}{\varepsilon}\kappa\left(J^{**} - n^{k+1}u^{k+1}\right). \end{aligned} \tag{16}$$

Eliminating J^{**} yields

$$u^{k+1} + \frac{\frac{1}{\Delta t} + \frac{\alpha}{\varepsilon}}{\frac{\rho^{k+1}}{\Delta t} + \frac{\alpha}{\varepsilon}\left(\rho^{k+1} + \kappa n^{k+1}\right)}\Delta t \nabla_x p^{k+1} = \frac{\left(\frac{1}{\Delta t} + \frac{\alpha}{\varepsilon}\right)\rho^{k+1}u^* + \frac{\alpha}{\varepsilon}\kappa J^*}{\frac{\rho^{k+1}}{\Delta t} + \frac{\alpha}{\varepsilon}\left(\rho^{k+1} + \kappa n^{k+1}\right)}. \tag{17}$$

DOI: 10.1002/fld

Taking the divergence on both sides, because u^{k+1} is divergence free, one arrives at

$$\nabla_x \cdot \left(\frac{1}{\rho_\varepsilon^{k+1}} \nabla_x p^{k+1} \right) = \frac{1}{\Delta t} \nabla_x \cdot \left(\frac{\rho^{k+1}}{\rho_\varepsilon^{k+1}} u^* + \frac{\frac{\alpha}{\varepsilon}}{\frac{1}{\Delta t} + \frac{\alpha}{\varepsilon}} \kappa \frac{J^*}{\rho_\varepsilon^{k+1}} \right), \qquad \frac{\partial p^{k+1}}{\partial \hat{\nu}} |_{\partial\Omega} = 0, \quad (18)$$

where we have set

$$\rho_\varepsilon^{k+1} := \frac{\frac{\rho^{k+1}}{\Delta t} + \frac{\alpha}{\varepsilon} \left(\rho^{k+1} + \kappa n^{k+1} \right)}{\frac{1}{\Delta t} + \frac{\alpha}{\varepsilon}}. \quad (19)$$

The pressure p^{k+1} is obtained by solving the variable coefficient Poisson equation (18). Again, its discretization can be solved by the Conjugate Gradient method. Then, u^{k+1} is obtained from (17) and thus J^{**} by (16).

As far as the first order method is concerned, α can be chosen arbitrarily in $(0, 1)$; in practice, we set $\alpha = 1/2$. As it is usual with variable density flows, pressure and velocity are obtained by solving discrete Helmholtz or Poisson systems with variable coefficients. These matrices need to be re-assembled at each time step.

Step 3: Kinetic equation. The particle distribution function f^{k+1} is calculated from the kinetic equation (1), with a fully implicit treatment of the Fokker–Planck operator

$$\frac{f^{k+1} - f^k}{\Delta t} + v \cdot \nabla_x f^k - \nabla_x \Phi \cdot \nabla_v f^k = \frac{1}{\varepsilon} L_{u^{k+1}} f^{k+1}, \quad (20)$$

where

$$L_{u^{k+1}} f^{k+1} = \nabla_v \cdot \left(\left(v - u^{k+1} \right) f^{k+1} + \nabla_v f^{k+1} \right).$$

We apply the technique introduced in [20] to solve this system: it allows to write the discrete version of the Fokker–Planck operator as a symmetric linear system, which can thus be solved with efficient methods.

2.2. A second order scheme

The accuracy with respect to the time variable can be improved to second order using backward differentiation formula, following the technique introduced in [1].

Let us now detail what the scheme for the fluid–particles system becomes. We shall use the shorthand notation $a^\dagger = 2a^k - a^{k-1}$.

Step 1: Advancing densities. The densities n^{k+1} and ρ^{k+1} are given by

$$\begin{aligned} \frac{1}{2\Delta t} \left(3n^{k+1} - 4n^k + n^{k-1} \right) &= - \int v \cdot \nabla_x f^\dagger \, \mathrm{d}v, \\ \frac{1}{2\Delta t} \left(3\rho^{k+1} - 4\rho^k + \rho^{k-1} \right) &= -\nabla_x \cdot (\rho u)^\dagger. \end{aligned} \quad (21)$$

Step 2: Updating moments. To ensure both the AP property and the second order accuracy, we include the stiff terms in both the pressureless and the projection steps, but only $O(\Delta t)$ of the stiff terms are left to the projection step. We thus set

$$\alpha = \frac{\Delta t}{t_{\max}},$$

where $t_{\max}$ is the final time of simulation.

Step 2.1: Pressureless step.

$$\frac{1}{2\Delta t} \left(3J^* - 4J^k + J^{k-1} \right) = - \int v \otimes v \nabla_x f^\dagger \, \mathrm{d}v - n^\dagger \nabla_x \Phi - \frac{1-\alpha}{\varepsilon} \left(J^* - n^{k+1} u^* \right), \quad (22a)$$

DOI: 10.1002/fld

$$\frac{1}{2\Delta t}\left(3\rho^{k+1}u^* - 4\rho^k u^k + \rho^{k-1}u^{k-1}\right) - \Delta_x u^* + \nabla_x p^k = -\nabla_x \cdot (\rho u \otimes u)^\dagger + \frac{1-\alpha}{\varepsilon}\kappa\left(J^* - n^{k+1}u^*\right). \tag{22b}$$

Step 2.2: Projection step. The pressure is obtained from the system

$$\frac{3}{2\Delta t}\left(J^{**} - J^*\right) = -\frac{\alpha}{\varepsilon}\left(J^{**} - n^{k+1}u^{k+1}\right),$$
$$\frac{3}{2\Delta t}\left(\rho^{k+1}u^{k+1} - \rho^{k+1}u^*\right) + \nabla_x\left(p^{k+1} - p^k\right) = \frac{\alpha}{\varepsilon}\kappa\left(J^{**} - n^{k+1}u^{k+1}\right).$$

Step 3: Kinetic equation. Finally, solve

$$\frac{3f^{k+1} - 4f^k + f^{k-1}}{2\Delta t} + (v\cdot\nabla_x - \nabla_x\Phi\cdot\nabla_v)\left(2f^k - f^{k-1}\right) = \frac{1}{\varepsilon}L_{u^{k+1}}f^{k+1}, \tag{23}$$

and, then the moments n^{k+1} and J^{k+1} are obtained from definition (9).

We will check on numerical experiments the convergence order of the scheme (21)–(23) in Section 3. This second order scheme is a multistep method. To compute the solutions at t^{k+1}, one needs the solutions from both t^k and t^{k-1}. Because the information is not available initially, one should start at least for a single time step with the first order scheme.

2.3. The asymptotic-preserving property

Following the same argument as in [1], one can obtain, as $\varepsilon \to 0$, the following limit scheme from the first order method (12)–(20):

$$\begin{cases} \frac{1}{\Delta t}\left(n^{k+1} - n^k\right) = -\nabla_x\cdot\left(n^k u^k\right), \\ \frac{1}{\Delta t}\left(\rho^{k+1} - \rho^k\right) = -\nabla_x\cdot\left(\rho^k u^k\right), \\ \frac{1}{\Delta t}\left(\left(\rho^{k+1} + \kappa n^{k+1}\right)u^* - \left(\rho^k + \kappa n^k\right)u^k\right) - \Delta_x u^* = \\ \qquad -\nabla_x\cdot\left(\left(\rho^{k+1} + \kappa n^k\right)u^k \otimes u^k\right) - \kappa\nabla_x n^k - \kappa n^k\nabla_x\Phi + O(\varepsilon), \\ u^{k+1} + \frac{1}{\rho^{k+1} + \kappa n^{k+1}}\Delta t\nabla_x p^{k+1} = u^*, \\ \nabla_x\cdot u^{k+1} = 0. \end{cases} \tag{24}$$

It is exactly the first order projection step for the limiting system (11), which is mainly the INS system with the space variable density $(\rho + \kappa n)$.

Similarly, the limit of the second order scheme (21)–(23), as $\varepsilon \to 0$, formally gives

$$\begin{cases} \frac{1}{2\Delta t}\left(3n^{k+1} - 4n^k + n^{k-1}\right) = -\nabla_x\cdot\left(n^k u^k\right)^\dagger, \\ \frac{1}{2\Delta t}\left(3\rho^{k+1} - 4\rho^k + \rho^{k-1}\right) = -\nabla_x\cdot\left(\rho^k u^k\right)^\dagger, \\ \frac{1}{2\Delta t}\left(3\left(\rho^{k+1} + \kappa n^{k+1}\right)u^* - 4\left(\rho^k + \kappa n^k\right)u^k + \left(\rho^{k-1} + \kappa n^{k-1}\right)u^{k-1}\right) - \Delta_x u^* + \nabla_x p^k = \\ \qquad -\nabla_x\cdot((\rho + \kappa n)u \otimes u)^\dagger - \kappa\nabla_x n^\dagger - \kappa n^\dagger\nabla_x\Phi, \\ \frac{3\left(u^{k+1} - u^*\right)}{2\Delta t} + \frac{1}{\rho^{k+1} + \kappa n^{k+1}}\nabla_x\left(p^{k+1} - p^k\right) = 0, \\ \nabla_x\cdot u^{k+1} = 0, \end{cases} \tag{25}$$

which is a second order projection method for the limiting system (11).

DOI: 10.1002/fld

Remark 2.1
The second order projection methods for the INS system with variable fluid density have been studied in [22], which used a combination of midpoint method and Crank–Nicolson method in time discretization. Here, we derive a different method that is based on a backward differentiation formula type discretization in time. However both methods are natural generalizations of the projection method because the problem is reformulated such that one only needs the Helmholtz solvers for u and a variable coefficient Poisson solver for p.

2.4. Full discretization and general comments

We refer to the relevant sections in [1] for the details on space and velocity discretization, as well as the inversion of the Fokker–Planck operator.

The mass conservation for the fluid (the first equation in (3)) is not include in [1]. In the present situation, it turns out to be natural to use a kinetic scheme, as we did in [2] when dealing with compressible flows. A consequence of this is that, in the limit system, the mass conservation equations for the particles and the dense phase are discretized with the same method. Namely, we solve

$$\frac{\rho^{k+1}-\rho^k}{\Delta t} = -\int_{\mathbb{R}^N} v\cdot\nabla_x\left(\rho^k e^{-|v-u^k|^2/2}\right)\frac{\mathrm{d}v}{(2\pi)^{N/2}},$$

and for space discretization, we approximate the convection operator $v\cdot\nabla_x$ dimension-by-dimension by upwind techniques (at first order or with second order MUSCL methods including slope limiters, see [23]). The momentum equations for the fluid are solved by using a second order central difference on the transport part. We can use a kinetic scheme as well for the convection terms of the fluid momentum equation: the limiting scheme would be exactly the kinetic scheme for the limiting system (11). In this case, note that the second moment $\int_{\mathbb{R}^N} v\, v\cdot\nabla_x\left(\rho^k e^{|v-u^k|^2/2}\right)\frac{\mathrm{d}v}{(2\pi)^{N/2}}$ introduces a pressure term, proportional to ρ^k.

We point out that, owing to the divergence free condition, the fluid density ρ (and the two macroscopic densities n and ρ for the limit problem) fulfills the maximum principle: if $0<\underline{\rho}\leqslant\rho(0,x)\leqslant\bar{\rho}<\infty$ initially, then $0<\underline{\rho}\leqslant\rho(t,x)\leqslant\bar{\rho}<\infty$ holds for any positive time. Here, in the Cartesian grids, we use Finite Difference approximation so that these discretization described above are enough to guarantee this property. However, working on general tessellations might require more refined methods in order to preserve the natural estimates on the fluid density: for such intricate coupling, violating the maximum principle on ρ might compromise the stability of the whole simulation, see for further details [24] on these delicate issues.

The scheme can be interpreted as a *predictor–corrector* method: the momentum of particles is first predicted by J^* and J^{**}, then corrected to J^{k+1} after f^{k+1} is solved. We point out that the main computational cost consists precisely in updating f^{k+1} because the equation involves both x and v variables (one needs to invert a system in v at each x). With the prediction–correction trick however, we determine first macroscopic quantities, and the Fokker–Planck system has to be solved only once per time step. The remarkable feature of this multiphase scheme is the fact that the overall cost corresponds to solving two single phase systems and even for the second order scheme only need to invert once the single phase Fokker–Planck equation. The stability analysis of the complete problem is beyond the scope of this paper. However, we can expect, and as confirmed by our numerical observations, that the only constraint on the time step is the CFL condition coming from the transport part of the kinetic equation (1), that is $\Delta t\leqslant\frac{\Delta x}{\max|v|}$, with Δx the space mesh size.

Remark 2.2
An alternative treatment of the Fokker–Planck operator is presented in [25, Chap. 12]. This scheme relies on a tricky combination of spectral analysis with a well-balanced treatment of the convection term. It leads to a suitable definition of the numerical fluxes corresponding to $v\cdot\nabla_x f$. (Note that this step needs the inversion of a certain linear system.) In turn, an efficient scheme for the Fokker–Planck equation is obtained, which is stable under the usual transport stability condition. This idea is adapted in [25, Section 12.4] to deal with a simple 1D fluid-particle problem where the fluid is supposed homogeneous and the velocity obeys the Burgers equation. The well-balanced fluxes are

DOI: 10.1002/fld

then obtained by decoupling the two phases. It would be interesting to discuss the ability of this method to handle stiff drag forces and to extend it to more complex multidimensional flows.

3. NUMERICAL SIMULATIONS

Let us now check the performances of the method through a set of numerical experiments. We propose simulations on the two-dimensional setting: from now on, we denote $\mathbf{x} = (x, y)$ the position variable, $\mathbf{v} = (v_1, v_2)$ the velocity variable, $\mathbf{u} = (u_1, u_2)$ the fluid velocity, and $\mathbf{u}_p = (u_{p1}, u_{p2}) = J/n$ the macroscopic particle velocity. Unless otherwise specified, simulations are performed under the following numerical conditions:

- The computational domain is defined by $\mathbf{x} \in [0,1]^2$. For the velocity variable, we use the truncated domain $\mathbf{v} \in [-v_{\max}, v_{\max}]^2$, with $v_{\max} = 6$. As in [1], we use a regular and symmetric velocity grid. We work with $N_x = 128$ grid points in each space direction and $N_v = 32$ grid points in each velocity direction.
- We make use of the following boundary conditions

  Specular reflection for particles f,
  No-slip for the fluid velocity u,
  Neumann boundary condition for the pressure p.

  When necessary, a Neumann-like boundary condition is applied on the fluid density ρ.
- We apply the second order method described in Section 2.2. The van Leer type slope limiter (see [26]) is applied on the discretization of the advection operators.
- The time step is determined by $\Delta t = \frac{\Delta x}{5 v_{\max}}$, which guarantees the stability.
- The initial particle distribution function is defined by

$$f(0, \mathbf{x}, \mathbf{v}) = n(0, \mathbf{x}) M_{\mathbf{u}_p(0,\mathbf{x})},$$

  with various expressions for the macroscopic density $n(0, x)$. Notice that it is not an equilibrium state when $\mathbf{u}_p \neq \mathbf{u}$ and thus $L_{\mathbf{u}} f \neq 0$ in (2).
- For the coupling parameter, we take $\kappa = 2$ throughout the simulations. We point out that we made a couple of runs with far larger values of κ, without encountering any difficulty.
- The gravity is taken into account: it points downwards and we set $g = 1$. The Reynolds number is set to $\mathrm{Re} = 1000$.

The first question is to determine whether or not the treatment of fluid inhomogeneities degrades the accuracy of the scheme reported for the homogeneous case and to check the AP property. Hence, we work with initial data defined as in [1], up to fluid homogeneities ($\rho(0, x) = 1$ in [1]), namely

$$\begin{aligned} n(0,\mathbf{x}) &= 10^{-10} + \exp\left(-80(x-0.5)^2 - 80(y-0.5)^2\right), \\ \mathbf{u}_p(0,\mathbf{x}) &= \begin{pmatrix} \sin^2(\pi x)\sin(2\pi y) \\ -\sin^2(\pi y)\sin(2\pi x) \end{pmatrix}, \\ \rho(0,\mathbf{x}) &= 1 + \exp\left(-40(x-0.5)^2 - 40(y-0.5)^2\right), \\ \mathbf{u}(0,\mathbf{x}) &= \mathbf{u}_p(0,\mathbf{x}). \end{aligned} \tag{26}$$

We vary the mesh size: we set $\Delta x = \frac{1}{N_x}$ with $N_x = 16, 32, 64,$ and128, respectively, and use $N_v = 32$. Denote $f_{\Delta x}$, $\rho_{\Delta x}$, and $\mathbf{u}_{\Delta x}$ the corresponding numerical solution. Given a discrete quantity φ, at the final time $t_{\max} = 0.025$, we evaluate the relative error in ℓ^p norm

$$e_{\Delta x}(\varphi) = \max_{t \in (0, t_{\max})} \frac{||\varphi_{\Delta x}(t) - \varphi_{2\Delta x}(t)||_p}{||\varphi_{2\Delta x}(0)||_p}. \tag{27}$$

We bear in mind that the stability constraint imposes $\Delta t = O(\Delta x)$. We shall say that the numerical scheme is of order k if $e_{\Delta x} \leqslant C \Delta x^k$ holds. Here, simulations are performed with the Reynolds number $\mathrm{Re} = 1$ (higher values can not be resolved on the coarse grid $N_x = 16$). Evaluation of the ℓ^1 norm of the particle distribution f and of the ℓ^2 norm of the fluid density ρ and velocity $\mathbf{u}$ is reported

DOI: 10.1002/fld

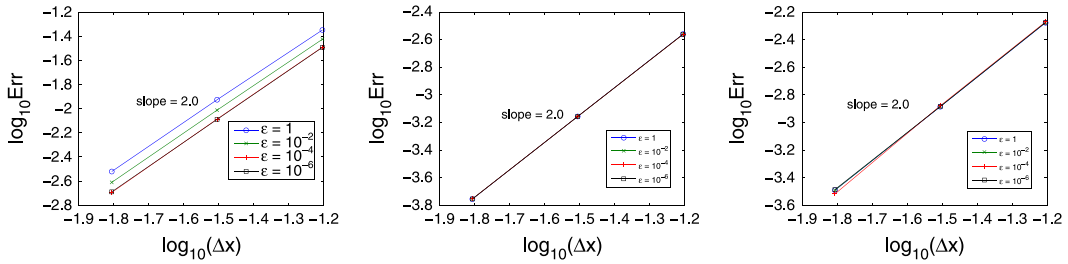

(a) Particle distribution f. (b) Fluid density ρ. (c) Fluid velocity $\mathbf{u}$.

Figure 1. Convergence order of the second order method with the initial data (26): l^1 errors (27) of the particle distribution f (a), l^2 errors of fluid density ρ (b), and fluid velocity $\mathbf{u}$ (b) with different ε.

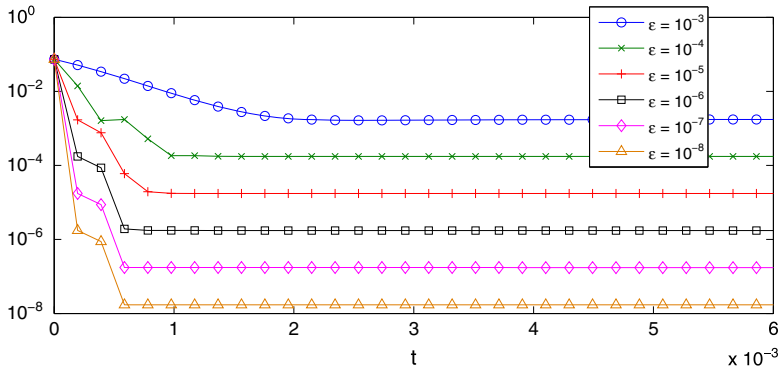

Figure 2. Time evolution of $||f - nM_{\mathbf{u}}||_1$ with different ε, starting with the initial data (28).

in Figure 1. We obtain the second order accuracy: on the one hand, the fluid density is captured with the required accuracy, and on the other hand, taking into account fluid inhomogeneities does not affect the quality of the results in comparison to the constant case, reported in [1].

Next, we turn to the AP property, comparing simulations by varying the scaling parameter ε. Again, we choose conditions similar to those of [1], by considering the following volcano like initial data

$$\begin{aligned} n(0,\mathbf{x}) &= \left(0.5 + 100\left((x-0.5)^2 + (y-0.5)^2\right)\right)\exp\left(-40(x-0.5)^2 - 40(y-0.5)^2\right), \\ \mathbf{u}_p(0,\mathbf{x}) &= \begin{pmatrix} -\sin(2\pi(y-0.5)) \\ \sin(2\pi(x-0.5)) \end{pmatrix}\exp\left(-20(x-0.5)^2 - 20(y-0.5)^2\right), \\ \mathbf{u}(0,\mathbf{x}) &= 0. \end{aligned} \tag{28}$$

Now, the fluid density is assumed inhomogeneous initially

$$\rho(0,\mathbf{x}) = 1.0 + \exp(-40(x-0.5)^2 - 40(y-0.5)^2).$$

The evolution of the norm $||f - nM_{\mathbf{u}}||_1$ where $M_{\mathbf{u}}$ is a Maxwellian centered at the fluid velocity $\mathbf{u}$ is depicted in Figure 2. The result verifies the AP property $f - nM_{\mathbf{u}} = O(\varepsilon)$ after one time step.

3.1. Some applications

In this section, our schemes are extended to more complicated circumstances. We deal with a couple of situations to demonstrate the ability of the method to reproduce desired physical phenomena. We show that the model exhibits interesting structure formation, because of the interaction between the two phases, with phenomena specifically related to fluid inhomogeneities.

DOI: 10.1002/fld

3.1.1. Dust eruption. The first test is concerned with the simulation of dust eruption, a toy model for the eruption of volcanic ash. Particles are injected from the bottom with constant velocity. The fluid is assumed initially at rest and linearly stratified, with a density decaying as altitude increases. More specifically, the initial conditions are given by

$$\begin{aligned} n(0,\mathbf{x}) &= 10^{-10}, \\ \rho(0,\mathbf{x}) &= \frac{3}{2} - \frac{y}{2}, \\ \mathbf{u}_p(0,\mathbf{x}) &= \mathbf{u}(0,\mathbf{x}) = \mathbf{0}. \end{aligned} \tag{29}$$

The injection domain Γ_b is defined by

$$\Gamma_b = \{(x,0) | 0.45 \leqslant x \leqslant 0.55\},$$

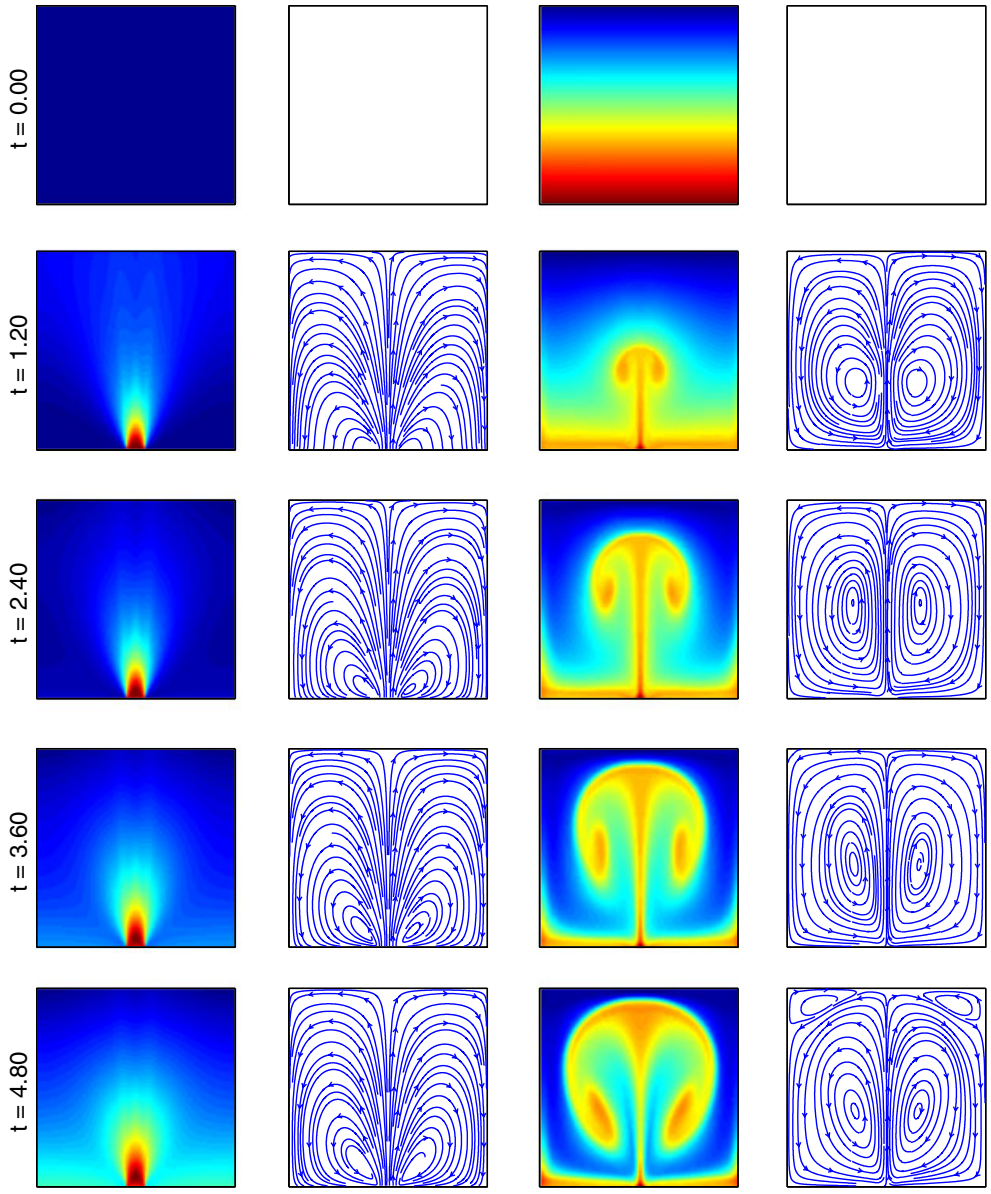

Figure 3. The time evolution of dust eruption. From left to right: the particle density, streamlines of particles velocities, fluid density, and streamlines of velocities of fluid. The Reynolds number is Re = 1000. (a) $\varepsilon = 1$.

DOI: 10.1002/fld

and we modify the specular reflection law on Γ_b by imposing the following incoming flux

$$f(t, \mathbf{x}, \mathbf{v}) = 1_{2 \leqslant v_2 \leqslant 3}, \quad \text{if } \mathbf{x} \in \Gamma_b$$

where v_2 is the second component of $\mathbf{v}$. The system is simulated with several values of ε.

Figure 3(a) gives the time evolution of this system with $\varepsilon = 1$. The first column shows the snapshots of the particle density at different time. The injected particles reach the top of the box after a short time, then fall down and accumulate at the bottom because of the gravity effect. The third column shows the snapshots of the fluid density. The heavier fluid, which stays near the ground at beginning, goes up with the incoming particles and falls down because of gravity, thus exhibiting the typical mushroom shape, which is well captured by the scheme. The second and fourth columns give the streamlines of particles and fluid, respectively. They are quite different because the drag force between the two phases is not significant. The behavior turns out to be significantly different as ε decreases.

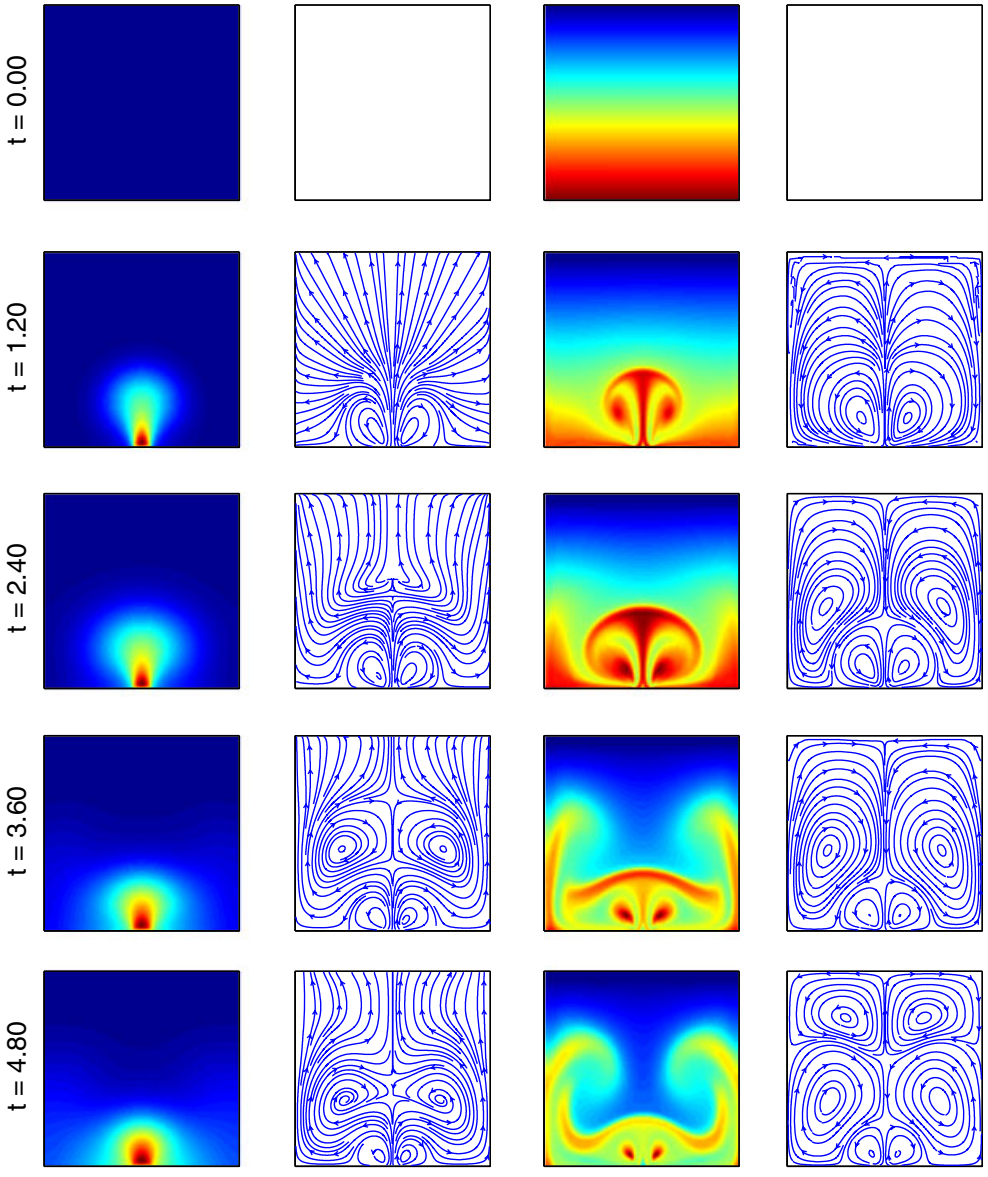

Figure 3. (Continued). (b) $\varepsilon = 10^{-2}$.

DOI: 10.1002/fld

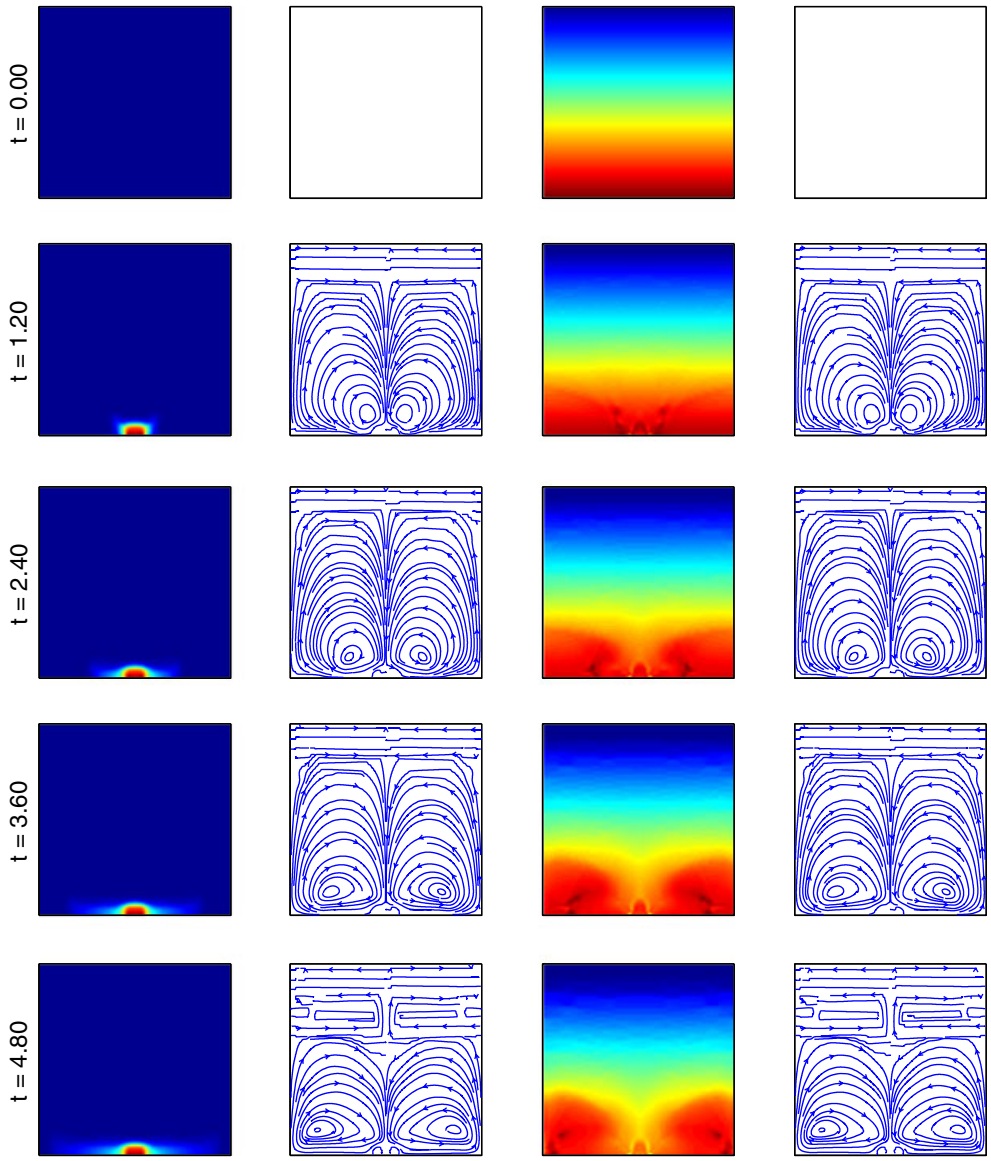

Figure 3. (Continued). (c) $\varepsilon = 10^{-6}$.

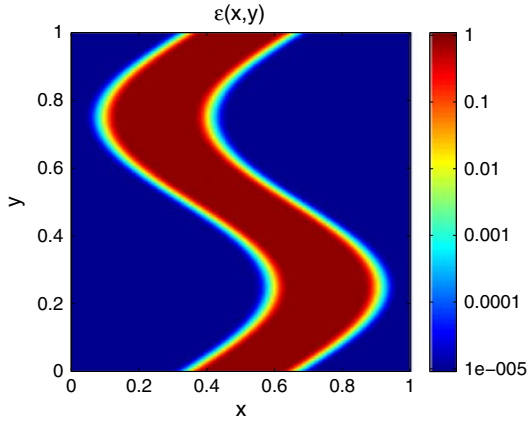

Figure 4. The **x**-dependent function $\varepsilon(\mathbf{x})$ given by (30), with $\varepsilon_0 = 10^{-5}$.

DOI: 10.1002/fld

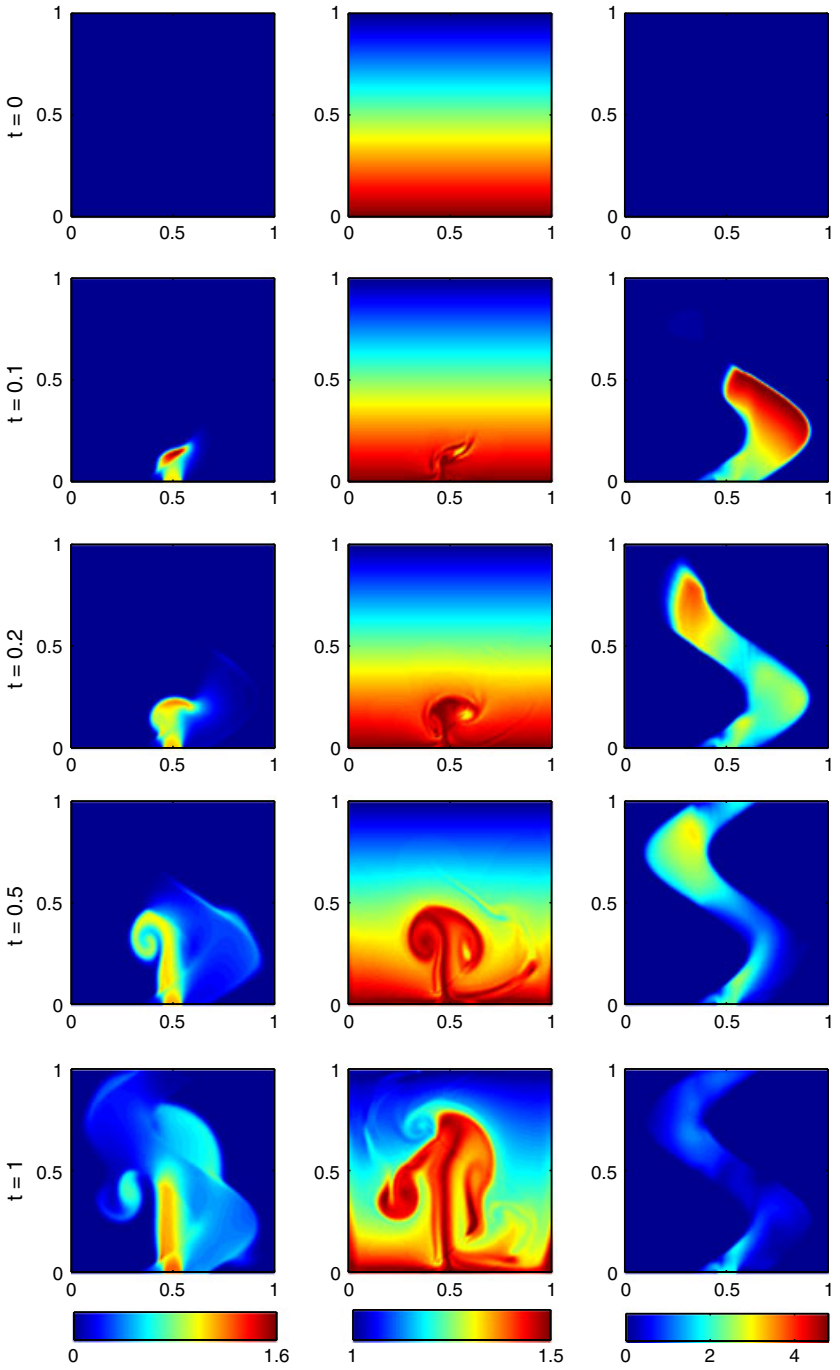

Figure 5. The time evolution of dust eruption problem in mixing regime. From left to right are the particle density, the fluid density, and the difference in their velocities $|\mathbf{u}_p - \mathbf{u}|$.

Figure 3(b) gives the time evolution of this system with $\varepsilon = 10^{-2}$. In this case, the drag force is stronger. The injected particles are slowed down by the fluid. Most particles fall back to the ground before reaching the top of the domain. The heavier fluid, which is blown away from the ground, can hardly go higher. The discrepancies between the streamlines of the particles and fluid are clearly reduced compared to the previous case.

Figure 3(c) gives the time evolution of this system with $\varepsilon = 10^{-6}$. The incoming particles stop moving up immediately because of the strong drag force and the gravity. A small portion of particles

DOI: 10.1002/fld

spreads on the ground. The heavier fluid always stays near the ground. The streamlines of the particles and fluid are quite similar to each other. We observe a clear splitting in the computational domain, with recirculation effects on the bottom and flat streamlines on the top.

3.1.2. Dust eruption in mixing regime. One of the advantages of AP schemes is that they can capture the solution behaviors automatically as ε varies in space. Using an example from [27], we consider a mixing regime problem, with an $\mathbf{x}$-dependent $\varepsilon(\mathbf{x})$,

$$\varepsilon(x,y) = \varepsilon_0 + \frac{1}{2}\left(\tanh\left(10 - 80\left(x - \frac{1}{2} - \frac{1}{4}\sin(2\pi y)\right)\right) + \tanh\left(10 + 80\left(x - \frac{1}{2} - \frac{1}{4}\sin(2\pi y)\right)\right)\right). \tag{30}$$

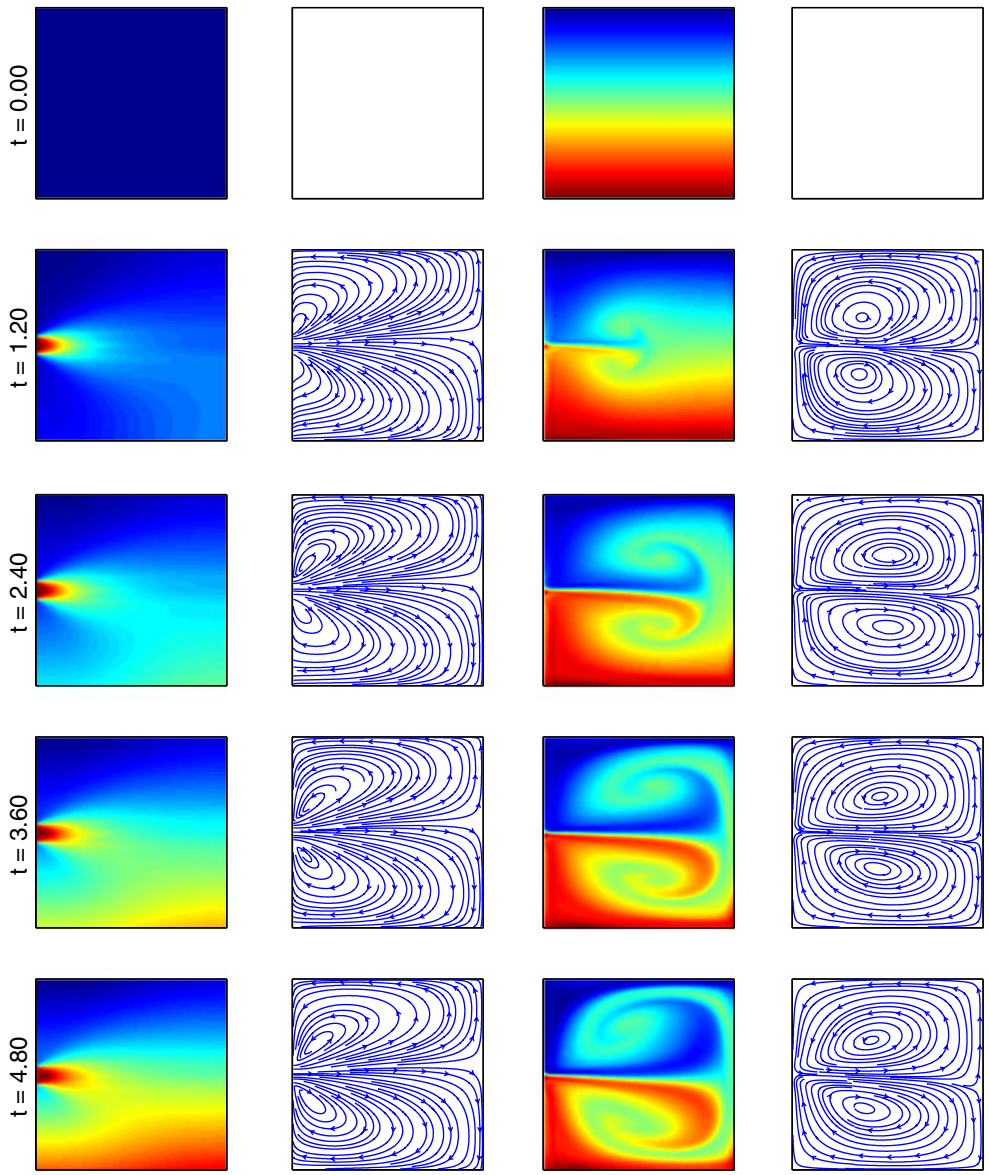

Figure 6. The time evolution of exhaust emission problem. From left to right: the particle density, streamlines of particles velocities, fluid density, and streamlines of velocities of fluid. The Reynolds number is Re = 1000. (a) $\varepsilon = 1$.

DOI: 10.1002/fld

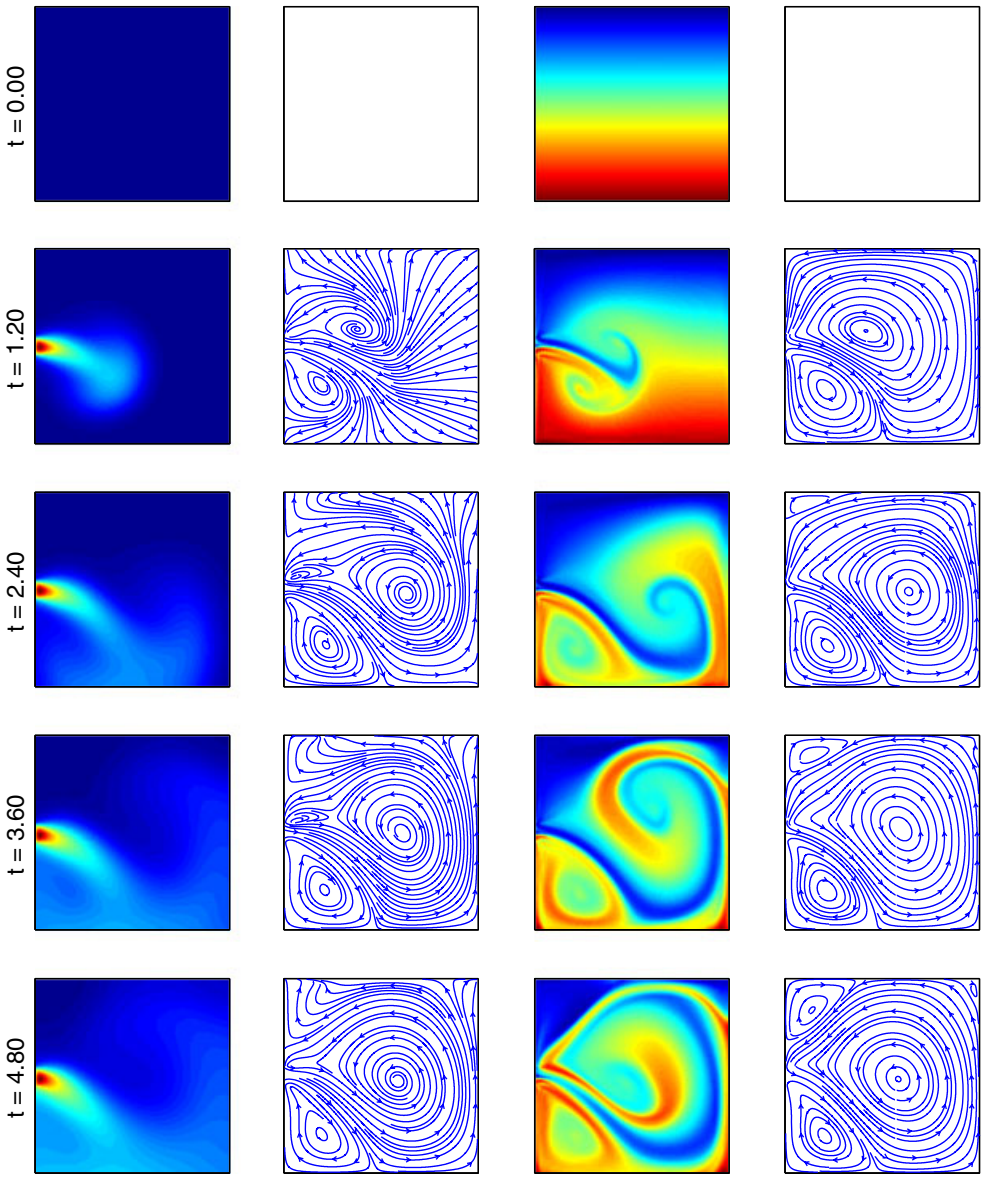

Figure 6. (Continued). (b) $\varepsilon = 10^{-2}$.

Here, $\varepsilon_0 \ll 1$ is a constant. $\varepsilon(\mathbf{x})$ varies from ε_0 to $O(1)$ smoothly, as shown in Figure 4 with $\varepsilon_0 = 10^{-5}$.

Now, we study the dust problem in this mixing regime. We use exactly the same physical and numerical parameters as in Section 3.1.1, except $\varepsilon(\mathbf{x})$. Similar to [1], we only discuss (30) as an evidence of feasibility, without diving into the discussion of the physical relevancy of working with spatially variable ε's.

Figure 5 shows several snapshots of the time evolution of the particle density, the fluid velocity, and the discrepancy of the two velocities $|\mathbf{u}_p - \mathbf{u}|$. Compared with Figure 3, the behaviors of both phases are clearly influenced by the spatially variable $\varepsilon(\mathbf{x})$. The difference of the velocities of two phases $|\mathbf{u}_p - \mathbf{u}|$ shows an S-shape profile, which is consistent to $\varepsilon(\mathbf{x})$ in Figure 4. This suggests that the fluid limit of this two-phase system is achieved automatically in the strong interaction regime where $\varepsilon \ll 1$. While in the weak interaction regimes where $\varepsilon = O(1)$, the two phases behave quite

DOI: 10.1002/fld

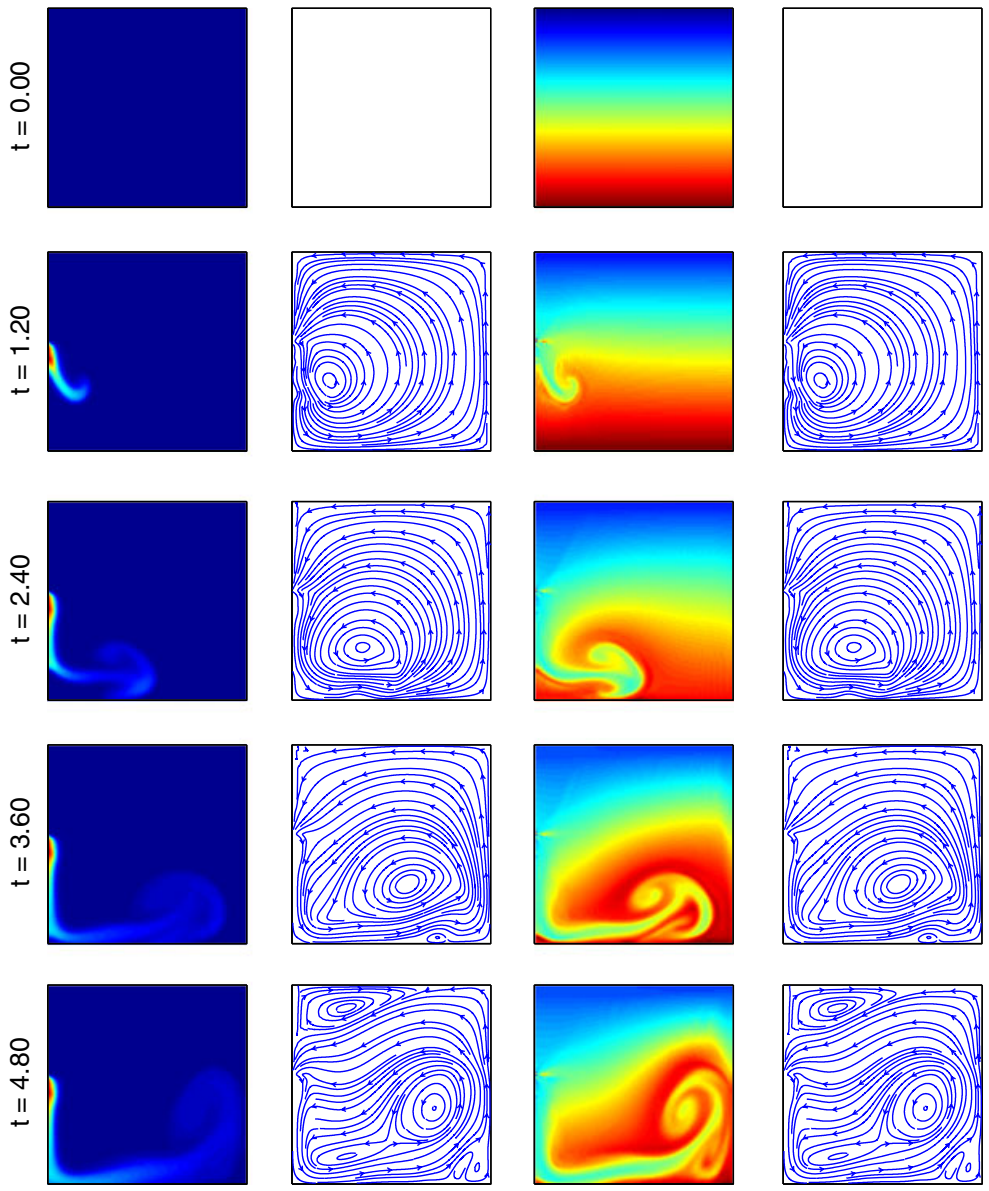

Figure 6. (Continued). (c) $\varepsilon = 10^{-6}$.

differently. Besides, $|\mathbf{u}_p - \mathbf{u}|$ decays as time evolves, which suggests that eventually the two-phase system approaches the global equilibrium (except in the region close to the entrance).

3.1.3. Exhaust emission/sewage outfall. In this simulation, particles are injected from the center of the left boundary with constant velocity. This can be seen as a toy model to simulate the exhaust emission from vehicles or the sewage outfall into the river/lake/sea. Initial and boundary conditions are the same as in (29) except that the boundary condition for the particles is now given by

$$f(t, \mathbf{x}, \mathbf{v}) = 1_{2 \leqslant v_1 \leqslant 3}, \quad \text{if } \mathbf{x} \in \Gamma_l, \tag{31}$$

where v_1 is the first component of $\mathbf{v}$ and the injection domain Γ_l is

$$\Gamma_l = \{(0, y) | 0.45 \leqslant y \leqslant 0.55\}.$$

DOI: 10.1002/fld

Figure 6(a) gives the time evolution of this system with $\varepsilon = 1$. The pictures from left to right give the particle density, the streamlines of particles velocities, the fluid density, and the streamlines of velocities of fluid, respectively. The injected particles reach the right end of the box after a short time, then fall down and accumulate at the right corner on the bottom because of the gravity effect. The circulation of the fluid is triggered. The upper half and lower half of the density evolve separately and behave like a typical cavity problem in both domains. Again, the streamlines of particles and fluid are quite different because the drag force between them is weak.

Figure 6(b) gives the time evolution of this system with $\varepsilon = 10^{-2}$. The incoming particles fall on the ground shortly after entering the box and then march on the ground. The fluid near the entrance

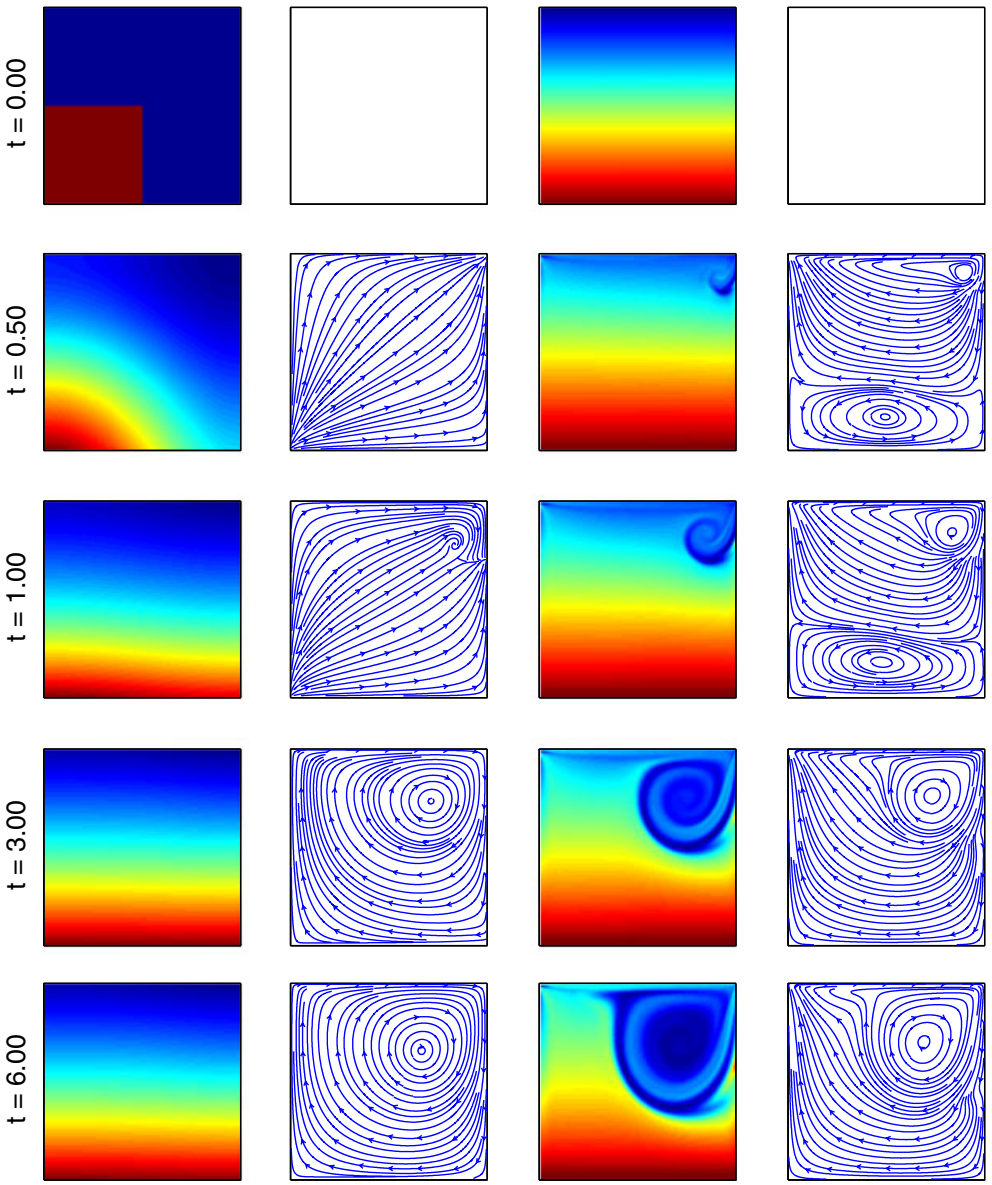

Figure 7. The time evolution of cavity problem. From left to right: the particle density, streamlines of particles velocities, fluid density, and streamlines of velocities of fluid. The Reynolds number is Re = 1000. (a) $\varepsilon = 1$.

DOI: 10.1002/fld

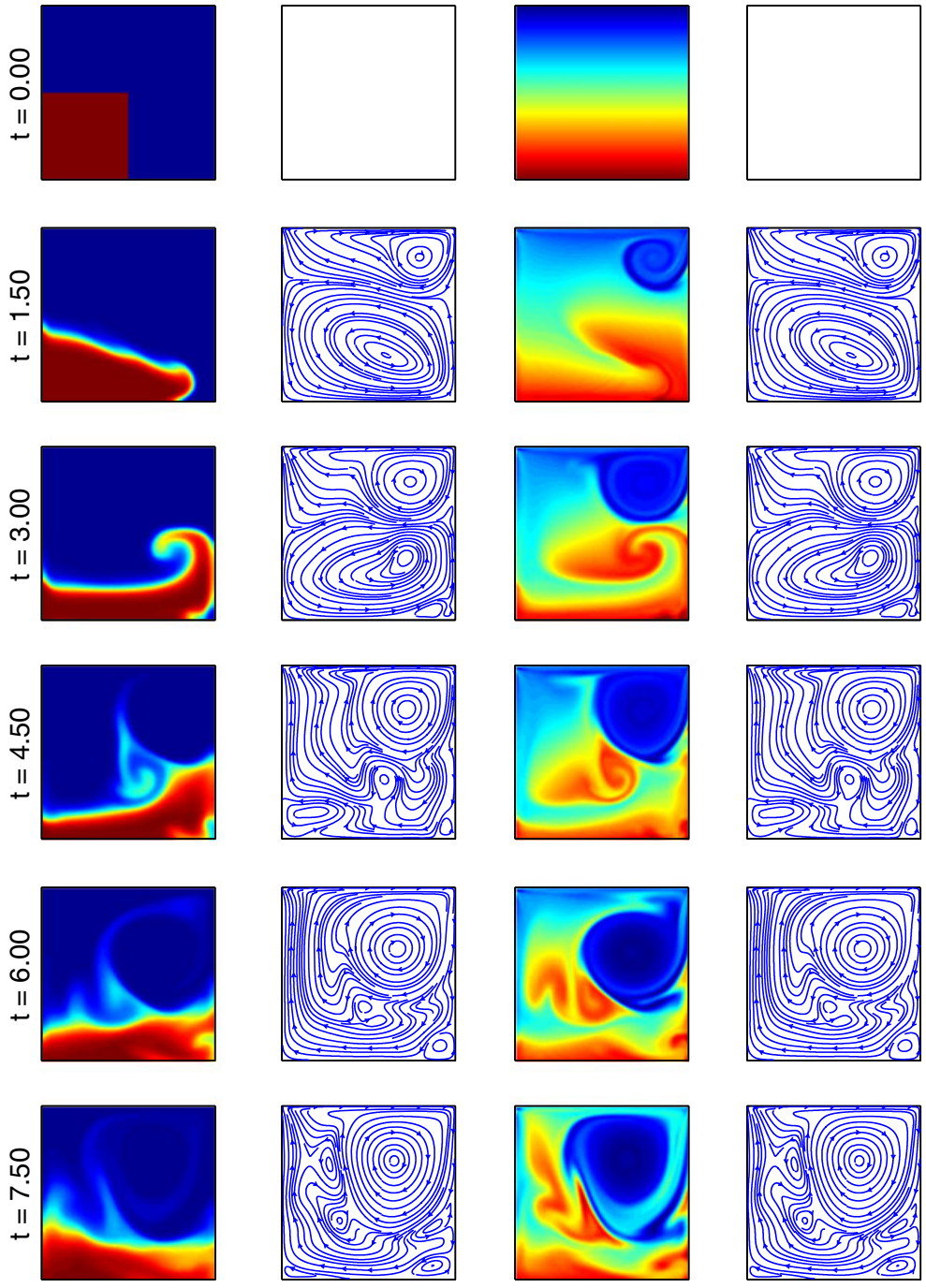

Figure 7. (Continued). (b) $\varepsilon = 10^{-8}$.

moves together with the particles, and later, the fluid in the whole domain gets mixed. Again, the streamlines of the particles and fluid are becoming similar.

Figure 6(c) gives the time evolution of this system with $\varepsilon = 10^{-6}$. Now, the drag force is very strong. The incoming particles move much slower so that they cannot reach the right end easily. The streamlines of the particles and fluid are almost the same.

In comparison to a similar test reported in [1], both the effect of gravity and the interplay between phases inhomogeneities modify significantly the features of the flow.

DOI: 10.1002/fld

3.1.4. The lid driven cavity problem. The last application is the lid driven cavity problem. The flow is driven by the lid, which moves to the right with a constant velocity. More specifically, the initial and boundary conditions are given by

$$\begin{aligned} n(0,\mathbf{x}) &= 10^{-10} + 1_{0\leqslant x\leqslant 0.5, 0\leqslant x\leqslant 0.5},\\ \rho(0,\mathbf{x}) &= \frac{3}{2} - \frac{y}{2},\\ \mathbf{u}_p(0,\mathbf{x}) &= \mathbf{u}(0,\mathbf{x}) = 0,\\ \mathbf{u}(t,\mathbf{x}) &= 0, \quad \text{if } \mathbf{x}\in\partial\Omega\backslash\Gamma_u,\\ \mathbf{u}(t,\mathbf{x}) &= (2,0)^T, \quad \text{if } \mathbf{x}\in\Gamma_u, \end{aligned} \tag{32}$$

where Γ_u is the top–boundary

$$\Gamma_u = \{(x,1)\}.$$

The specular boundary condition for f is applied. The system is also simulated with different ε.

Figure 7(a) gives the time evolution of this system with $\varepsilon = 1$. The particles spread to the right end because of the gravity and cover the bottom in a short time. The fluid circulates in the box because pdf the moving lid. The interaction between the two phases are not significant. The streamlines of particles and fluid are quite different.

Figure 7(b) gives the time evolution of this system with $\varepsilon = 10^{-8}$. The profiles of the two phases are much more complicated, because of the strong drag force. The streamlines of particles and fluid are exactly the same, suggesting that the two phases are moving together.

APPENDIX

Here, we prove the entropy dissipation inequality (4). Multiplying (1) by $1 + \Phi + v^2/2 + \ln(f)$ and integrating over $\mathbb{R}^N \times \mathbb{R}^N$, one obtains

$$\begin{aligned} &\frac{\mathrm{d}}{\mathrm{d}t}\left(\kappa\int_{\mathbb{R}^N\times\mathbb{R}^N} f\left(1+\Phi+v^2/2+\ln(f)\right)\,\mathrm{d}v\,\mathrm{d}x\right) + \int_{\mathbb{R}^N\times\mathbb{R}^N}\left(\Phi v\cdot\nabla_x f - \frac{v^2}{2}\nabla_x\Phi\cdot\nabla_v f\right)\mathrm{d}v\mathrm{d}x\\ &\quad = \frac{1}{\varepsilon}\int_{\mathbb{R}^N\times\mathbb{R}^N}\left(\frac{v^2}{2}+\ln f\right)L_u f\,\mathrm{d}v\mathrm{d}x. \end{aligned} \tag{A.1}$$

One can drop the second integration because

$$\int_{\mathbb{R}^N\times\mathbb{R}^N}\left(\Phi v\cdot\nabla_x f - \frac{v^2}{2}\nabla_x\Phi\cdot\nabla_v f\right)\mathrm{d}v\mathrm{d}x = \int_{\mathbb{R}^N\times\mathbb{R}^N}\left(\nabla_x\cdot(\Phi v f) - \nabla_v\cdot\left(\frac{v^2}{2}\nabla_x\Phi f\right)\right)\mathrm{d}v\mathrm{d}x = 0.$$

Next, multiplying the mass equation in (3) by Ψ and integrating over $\mathbb{R}^N$, one obtains,

$$\frac{\mathrm{d}}{\mathrm{d}t}\int_{\mathbb{R}^N}\rho\Psi\,\mathrm{d}x - \int_{\mathbb{R}^N}\nabla_x\Psi\cdot(\rho u)\,\mathrm{d}x = 0. \tag{A.2}$$

Multiplying the momentum equation in (3) by u and integrating over $\mathbb{R}^N$, one obtains,

$$\begin{aligned} &\frac{\mathrm{d}}{\mathrm{d}t}\int_{\mathbb{R}^N}\frac{1}{2}\rho|u|^2\,\mathrm{d}x + \frac{1}{\mathrm{Re}}\int_{\mathbb{R}^N}|\nabla_x u|^2\mathrm{d}x + \int_{\mathbb{R}^N}\nabla_x\Psi\cdot(\rho u)\mathrm{d}x\\ &\qquad = \frac{\kappa}{\varepsilon}\int_{\mathbb{R}^N\times\mathbb{R}^N} u\sqrt{f}\left((v-u)\sqrt{f} + 2\nabla_v\sqrt{f}\right)\mathrm{d}v\mathrm{d}x, \end{aligned} \tag{A.3}$$

where we have applied the incompressibility property of u.

Note that the Fokker–Planck operator (2) can be rewritten as

$$L_u f = \nabla_v\cdot\left(\sqrt{f}\left((v-u)\sqrt{f} + 2\nabla_v\sqrt{f}\right)\right).$$

DOI: 10.1002/fld

With integration by parts, one has

$$\begin{aligned}
\int_{\mathbb{R}^N} \frac{v^2}{2} L_u f \, \mathrm{d}v &= \int_{\mathbb{R}^N} -v\sqrt{f}\left((v-u)\sqrt{f} + 2\nabla_v\sqrt{f}\right)\mathrm{d}v,\\
\int_{\mathbb{R}^N} \ln f L_u f \, \mathrm{d}v &= \int_{\mathbb{R}^N} -\frac{\nabla_v f}{f}\sqrt{f}\left((v-u)\sqrt{f} + 2\nabla_v\sqrt{f}\right)\mathrm{d}v\\
&= \int_{\mathbb{R}^N} -2\nabla_v\sqrt{f}\left((v-u)\sqrt{f} + 2\nabla_v\sqrt{f}\right)\mathrm{d}v.
\end{aligned} \tag{A.4}$$

Then, (4) is proved by adding up (A.1)–(A.4).

ACKNOWLEDGEMENTS

This work was partially supported by NSF grants DMS-0608720, DMS-1114546, and NSF FRG grant DMS-0757285.

REFERENCES

1. Goudon T, Jin S, Liu JG, Yan B. Asymptotic-preserving schemes for kinetic–fluid modeling of disperse two-phase flows. *Journal of Computational Physics* 2013; **246**:145–164.
2. Goudon T, Jin S, Yan B. Simulation of fluid–particles flows: heavy particles, flowing regime and AP–schemes. *Communications in Mathematical Sciences* 2012; **10**:355–385.
3. Mathiaud J. Etude de systèmes de type gaz-particules. *Ph.D. Thesis*, ENS Cachan, 2006.
4. Murrone A, Villedieu P. Numerical modeling of dispersed two-phase flows. *AerospaceLab, The Onera Journal* 2011; **2**:1–13.
5. O'Rourke PJ. Collective drop effects on vaporizing liquid sprays. *Ph.D. Thesis*, Princeton Univ., 1981. Available as Technical Report #87545 Los Alamos National Laboratory.
6. Williams FA. *Combustion Theory* (2nd edition). Benjamin Cummings Publ.: Menlo Park, 1985.
7. Patankar NA, Joseph DD. Modeling and numerical simulation of particulate flows by the Eulerian–Lagrangian approach. *International Journal of Multiphase Flow* 2001; **27**:1659–1684.
8. Patankar NA, Joseph DD. Lagrangian numerical simulation of particulate flows. *International Journal of Multiphase Flow* 2001; **27**:1685–1706.
9. Baranger C, Boudin L, Jabin P-E, Mancini S. A modeling of biospray for the upper airways. *ESAIM: Proceedings* 2005; **14**:41–47.
10. Moussa A. Etude mathématique et numérique du transport d'aérosols dans le poumon humain. *Ph.D. Thesis*, ENS Cachan, 2009.
11. Prosperetti A, Tryggvason G. *Computational Methods for Multiphase Flows*. Cambridge Univ. Press: Cambridge, 2007.
12. Caflisch R, Papanicolaou G. Dynamic theory of suspensions with Brownian effects. *SIAM Journal on Applied Mathematics* 1983; **43**:885–906.
13. Carrillo JA, Goudon T. Stability and asymptotics analysis of a fluid-particles interaction model. *Communications in Partial Differential Equations* 2006; **31**:1349–1379.
14. Carrillo JA, Goudon T, Lafitte P. Simulation of fluid & particles flows: asymptotic preserving schemes for bubbling and flowing regimes. *Journal of Computational Physics* 2008; **227**(16):7929–7951.
15. Goudon T, Jabin P-E, Vasseur A. Hydrodynamic limit for the Vlasov–Navier–Stokes equations. II. Fine particles regime. *Indiana University Mathematics Journal* 2004; **53**(6):1517–1536.
16. Mellet A, Vasseur A. Global weak solutions for a Vlasov–Fokker–Planck/Navier–Stokes system of equations. *Mathematical Models and Methods in Applied Sciences* 2007; **17**(7):1039–1063.
17. Mellet A, Vasseur A. Asymptotic analysis for a Vlasov–Fokker–Planck/compressible Navier–Stokes system of equations. *Communications in Mathematical Physics* 2008; **281**(3):573–596.
18. Jin S. Efficient asymptotic-preserving (AP) schemes for some multiscale kinetic equations. *SIAM Journal on Scientific Computing* 1999; **21**(2):441–454.
19. Jin S. *Asymptotic preserving (AP) schemes for multiscale kinetic and hyperbolic equations: a review*, Lecture Notes for Summer School on "Methods and Models of Kinetic Theory" (M&MKT), Porto Ercole (Grosseto, Italy), June 2010. Rivista di Matematica della Universitã di Parma 2012; **3**:177–216.
20. Jin S, Yan B. A class of asymptotic-preserving schemes for the Fokker–Planck–Landau equation. *Journal of Computational Physics* 2011; **230**(17):6420 –6437.
21. Quarteroni A, Sacco R, Saleri F. *Numerical Mathematics* (Second Edition). Springer: Berlin Heidelberg, Germany, 2007.
22. Bell J, Marcus D. A second-order projection method for variable-density flows. *Journal of Computational Physics* 1992; **101**(2):334 –348.

DOI: 10.1002/fld

23. Perthame B. Second order Boltzmann schemes for compressible Euler equations in one and two space dimension. *SIAM Journal on Numerical Analysis* 1992; **29**(1):1–19.
24. Calgaro C, Chane-Kane E, Creusé E, Goudon T. L^∞-stability of vertex-based MUSCL finite volume schemes on unstructured grids; simulation of flows with high density ratios. *Journal of Computational Physics* 2010; **229**(17):6027–6046.
25. Gosse L. *Computing Qualitatively Correct Approximations of Balance Laws*, SIMAI Springer Series, vol. 2. Springer-Verlag New York: New York, 2013.
26. LeVeque RJ. *Numerical Methods for Conservation Laws*. Birkhauser-Verlag: Basel.
27. Filbet F, Jin S. A class of asymptotic–preserving schemes for kinetic equations and related problems with stiff sources. *Journal of Computational Physics* 2010; **229**(20):7625–7648.

DOI: 10.1002/fld